Nano Research

Open Access

Research Article

Carbon nanotube incorporation and framework protonation-regulated energy band for enhanced photocatalytic hydrogen peroxide production of COF

Luanying Yang, Wenxin Lv, Yueyue Wang, and Yi Wang ✉

Center for Advanced Low-dimension Materials, State Key Laboratory for Modification of Chemical Fibers and Polymer Materials, College of Chemistry and Chemical Engineering, Donghua University, Shanghai 201600, China

Cite this article: *Nano Research*, **2025**, *18*, 94907024. https://doi.org/10.26599/NR.2025.94907024

ABSTRACT: Covalent organic frameworks (COFs) were the promising solar catalysts for producing hydrogen peroxide (H_2O_2). However, they remain suffered from poor light absorption, slow charge separation, and limited substrate accessibility. To address these issues, we synthesized an imine-linked triazine-based COF directly onto carbon nanotubes (CNTs) through an interface-mediated Schiff base reaction, creating a tubular nano-complex designated as CNT@COF. Protonation of the imine bonds in the resulting CNT@COF-H significantly enhanced its photocatalytic H_2O_2 production, achieving a rate of 790.5 μM·h^{-1} under one sunlight irradiation. This performance outshines that of the unmodified COF and surpasses many other COF-based materials. Further studies revealed that protonation improved substrate accessibility, while the integrated CNTs acted as electron transporters to expand light absorption and reduce charge recombination, thereby enhancing photocatalytic activity. The efficacy of CNT@COF-H was demonstrated through its strong sterilization capability and clear dye degradation, offering a promising method for efficient and eco-friendly production of H_2O_2.

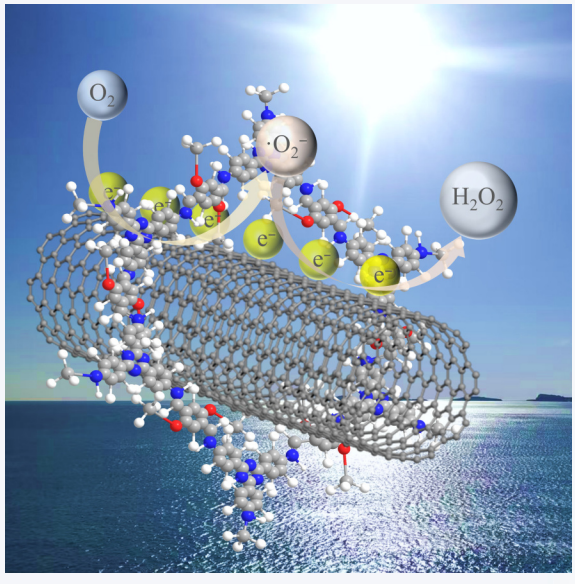

KEYWORDS: hydrogen peroxide, photocatalysis, covalent organic framework (COF)-based composites, solar light, charge separation

1 Introduction

Hydrogen peroxide (H_2O_2) stands as a pivotal chemical with wide applications ranging from disinfection and bleaching to serving as a green oxidant in chemical syntheses [1, 2]. Traditionally, anthraquinone production is the dominated process, but suffered from flammability inflammability and explosivity [3]. Alternatively, oxygen reduction reaction (ORR) or water oxidation reaction (WOR) presents a significant progress for H_2O_2 generation in recent years [4, 5]. Usually, this type of H_2O_2 evolution is an electrochemical process, which involves the consumption of electrical power and often suffers from electrode degradation over time. Comparatively, photocatalysis, particularly solar-driven photocatalysis, has emerged as a favorable alternative to electrochemical methods for H_2O_2 synthesis due to its escaping from external electrical power [6, 7]. Nevertheless, photocatalysis requires a catalyst to facilitate the reduction of molecular oxygen (O_2) or oxidative cleavage of water molecules to form H_2O_2 [8]. Generally, the photo catalyst absorbs incident light energy to produce electrons and holes in its conduction band and valence band [9, 10], respectively, where oxygen is reduced into H_2O_2 through one or two-electron transfer and H_2O is oxidized into H_2O_2 through the possible ·OH intermediate [11, 12]. Therefore, the efficiency of solar photocatalysis is heavily reliant on the performance of the catalysts used.

Traditional photocatalysts include precious metals [13], metal complexes [14], and semiconductors [15]. However, these materials are often expensive, and their production and disposal can lead to

Received: July 2, 2024; **Revised:** August 26, 2024
Accepted: September 4, 2024

✉Address correspondence to ywang@dhu.edu.cn

environmental concerns. Recently, covalent organic frameworks (COFs), on the other hand, have emerged as a promising class of materials for photocatalytic applications [16–19]. These are highly ordered, porous, and crystalline polymers constructed from organic building blocks linked by strong covalent bonds, which offer several advantages, including high surface area, tunable pore sizes, and the ability to modify their chemical functionality [20–22]. Their metal-free nature makes them more environmentally friendly than many traditional catalysts. The modularity of COFs allows for the design of materials with specific properties tailored to enhance photocatalytic performance, such as optimizing band gaps for light absorption and tailoring active sites for chemical reactions [23, 24]. However, COFs typically suffered from limited light-harvesting capability due to their intrinsic band gaps [25], which may not align with the solar spectrum. Meanwhile, the rate of charge separation and transfer within COFs was slow [26], limiting the generation of reactive species necessary for photocatalysis. Additionally, the dense nature of COFs also restricted the diffusion of substrates to the active sites, further impeding catalytic efficiency.

To circumvent these limitations, this work has focused on the development of a nanocomposite by coating the protonated imine-linked triazine-based COF on carbon nanotubes (CNTs). The resulting hybrid material, termed CNT@COF-H, ensures a strong interface between the two materials and combines the desirable properties of both components. The porous structure of COF remains accessible, providing ample active sites for the catalytic reactions. Especially, the protonated imine facilitates the accessibility of substrate (O_2 and H_2O) to the active sites. Meanwhile, the incorporated CNTs provide a conductive network that facilitates wide light adsorption and rapid electron transfer, enhancing the separation of electron–hole pairs generated upon light irradiation. As a result, a superior photocatalytic H_2O_2 generation to those of the pristine COF and many other reported COF-based materials was achieved in terms of increased H_2O_2 yield, good durability, and obvious sterilization/dye degradation ability. Therefore, this work promises a sustainable and cost-effective approach to harnessing solar energy for the chemical synthesis of H_2O_2, paving the way for greener and more efficient industrial processes (Scheme 1).

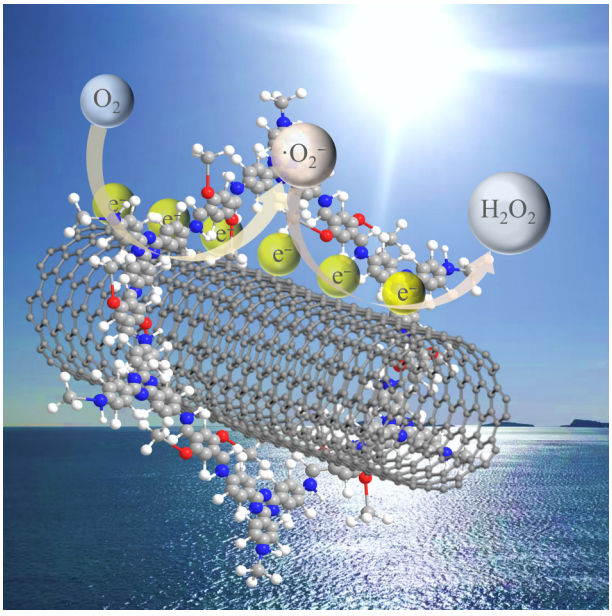

Scheme 1 Illustration for photocatalytic H_2O_2 production on CNT@COF-H.

2 Experimental

2.1 Preparation of TAPT-DMTP COF

8 mg of 2,5-dimethoxybenzene-1,4-dicarboxaldehyde (DMTP) and 20 mg of 1,3,5-tris-(4-aminophenyl)triazine (TAPT) were each dissolved in 10 mL of anhydrous acetonitrile. The solutions were then mixed, and acetic acid (500 μL) was added to the combined solution, which was allowed to react at ambient temperature and atmospheric pressure for 24 h. Upon completion of the reaction, the solution was centrifuged to collect the precipitate. This was washed three times with anhydrous ethanol and subsequently dried under vacuum to yield the COF material.

2.2 Preparation of COF-encapsulated CNT (CNT@COF) material

To synthesize CNT@COF, oxidized carbon nanotubes were initially produced. In a 200 mL round-bottom flask, 300 mg of carbon nanotubes were sonicated in 70 mL of 3.0 M HNO_3 at 60 °C for 15 min, then continuously for an additional 2 h. The resulting well-dispersed suspension was filtered and washed with deionized water to yield precipitates. These were then dispersed in 70 mL of 30% (v/v) H_2O_2 and subjected to the same oxidation process again. Afterward, the mixture was filtered, and the supernatant was washed until it reached a neutral pH. The oxidized CNTs, obtained after freeze-drying, were ultrasonically dispersed in anhydrous ethanol.

For the synthesis of CNT@COF, TAPT (20 mg) was dissolved in 10 mL of anhydrous acetonitrile. Then, the ethanol CNT solution (5 mL) was mixed into the TAPT solution and stirred at room temperature for 1 h. Subsequently, 10 mL of DMTP (8 mg) in acetonitrile and 500 μL of acetic acid were added. The mixture was stirred at room temperature for 24 h. Upon completion, the centrifuged precipitate was collected, washed thrice with anhydrous ethanol, and vacuum dried to acquire the CNT@COF material.

2.3 Protonation of COF-based materials

COF-based materials were protonated in ascorbic acid solutions. Typically, COF (5 mg) was ultrasonically dispersed in 5 mL of 0.1 M ascorbic acid solution for 5 min. The resulting product was then collected by centrifugation and dried overnight at 80 °C under vacuum to yield the ascorbic acid-modified COF. The protonation of CNT@COF was performed using the same method.

2.4 Photocatalytic generation of H_2O_2

The photocatalyst (5 mg) was ultrasonically dispersed in a 50 mL round-bottom beaker with 10 mL of deionized water. Oxygen was bubbled through the mixture for 30 min to achieve saturation and ensure full absorption by the material. It was then exposed to a xenon lamp light source (CEL-HXF300, Beijing Zhongjiao Jinyuan) equipped with a simulated sunlight spectral filter (AM1.5), at an optical power density of 0.1 W·cm^{-2}. Every 10 min, 1 mL of the mixture was sampled and centrifuged to separate the supernatant. From this, 0.5 mL was transferred to a 5 mL tube for hydrogen peroxide analysis using the iodometric method, where H_2O_2 can react with iodide and protons to form triiodide and water. To this sample, 2 mL of 0.1 M potassium iodide and 50 μL of 0.01 M

$(NH_4)_2MoO_4$ were added. After reacting for 5 min, the concentration of H_2O_2 was determined by measuring the absorbance at 352 nm with a ultraviolet–visible (UV–Vis) spectrophotometer.

$$H_2O_2 + 3I^- + 2H^+ \rightarrow 2H_2O + I_3^- \ (352\ nm)$$

3 Results and discussion

In the absence of CNT scaffolding, the imine-triazine COF synthesized through Schiff base reaction between TAPT and DMTP (Scheme S1 and Fig. S1 in the Electronic Supplementary Material (ESM)), and their protonated counterparts obtained by acidification in ascorbic acid, uniformly display echinoid-like nanospheres (Figs. 1(a) and 1(b)). The acidification process does not alter their morphology or size, maintaining an approximate diameter of 200 nm. Conversely, when utilizing carbon nanotubes as a scaffold (Fig. 1(c)), the resultant materials exhibit a one-dimensional tubular architecture (Figs. 1(d) and 1(e)), where smooth carbon nanotubes, with a diameter of about 12 nm, are encapsulated by a polymer layer approximately 34 nm thick, resulting in a structure reminiscent of snow-covered branches (Fig. 1(f)). The core of these branches is primarily composed of carbon, with a surface layer enriched in nitrogen and oxygen elements. X-ray diffraction (XRD) results for both the composite and its acidified version reveal characteristic diffraction peaks for carbon nanotubes (002) and the ordered structure of COF (100) [27], confirming the crystalline COF particles are enwrapped around the carbon nanotubes (Fig. 1(h)). Moreover, Raman spectroscopy (Fig. 1(i)) elucidates that the COF layer, composed of sp^2 hybridized carbon [28], sheathes the defect-laden surface of carbon nanotubes, with acidification leaving the ordered structure of the COF layer and the defect architecture of the inner carbon nanotubes unchanged. Compared to the TAPT and DMTP monomers, the COF and its carbon nanocomposite exhibit additional C=N stretching vibrations, indicating the COF layers are interconnected through imine bonds formed by the Schiff base reaction (Fig. 1(j)). At the same time, a new signal indexed as $C=NH^+$ further reveals that protonation predominantly occurs on the nitrogen atoms of imines and triazines, rendering the COF's color from light to dark with reversibility, i.e., it can be deprotonated under alkaline conditions (Figs. S2 and S3 in the ESM). Nitrogen adsorption–desorption isotherms (Fig. S4 in the ESM) and pore size distribution curves (Fig. 1(g)) indicate the presence of mesopores formed by slight stacking of carbon nanotubes. After encapsulation in COF, typical micropores of COFs (< 2 nm) emerge, accompanied by an increase in stacking pores. Protonation does not significantly alter the composite's pore structure, with its Brunauer–Emmett–Teller (BET) surface area and pore volume being 210.9 $m^2 \cdot g^{-1}$ and 0.167 $cm^3 \cdot g^{-1}$ (Table S1 in the ESM), respectively. These values showcased a hierarchically porous network structure formed by encapsulating CNTs with COFs. In this composite, thermogravimetric analysis reveals a COF content of approximately 77% and a carbon nanotube content of about 23%

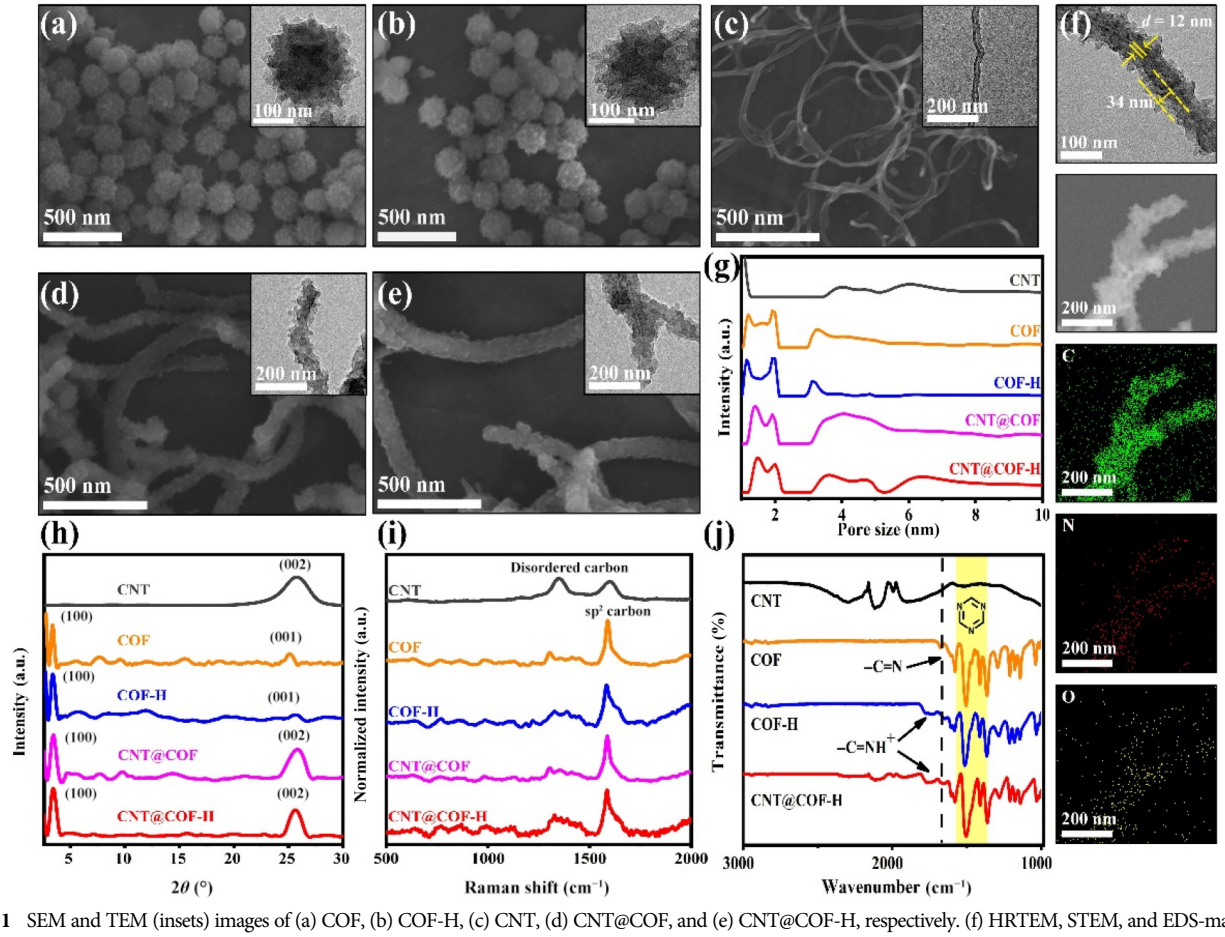

Figure 1 SEM and TEM (insets) images of (a) COF, (b) COF-H, (c) CNT, (d) CNT@COF, and (e) CNT@COF-H, respectively. (f) HRTEM, STEM, and EDS-mappings of CNT@COF-H for C, N, and O elements, respectively. (g) Pore size distribution curves, (h) XRD patterns, (i) Raman spectra, and (j) FTIR spectra of different materials.

(Fig. S5 in the ESM).

To further elucidate the tubular composite's structure, additional characterizations were performed. Compared to pure carbon nanotubes, the composite exhibits an additional N 1s signal, confirming the imine COF encapsulation of CNTs. Protonation does not affect the primary composition of carbon, oxygen, and nitrogen elements (Fig. 2(a), and Table S2 in the ESM). High-resolution C 1s spectra affirm that CNT@COF-H primarily comprises the C–C/C=C backbone from carbon nanotubes complexed with imine COF. Post-protonation, no significant shifts in C 1s peaks occur, indicating that protonation does not take place on carbon atoms (Fig. 2(b)). Comparatively, N 1s spectra of carbon nanotubes and the composite further verify COF coverage on the carbon nanotube surface. Notably, before protonation, the composite's nitrogen primarily originates from imine bonds and triazine rings' pyridinic nitrogen. After protonation, a new signal for protonated nitrogen appears, suggesting that protonation occurs in nitrogen-containing groups (Fig. 2(c)). The ^{13}C solid-state nuclear magnetic resonance (NMR) characterization displays distinct signals for imine bonds and triazine rings (Fig. 2(d)), reaffirming the presence of triazine-based imine COFs formed by Schiff base reactions. Encapsulation on CNT surfaces and subsequent protonation do not alter the main structure. However, chemical shift signals for carbon in imine bonds and triazine rings split into two distinct peaks, indicating that protonation occurs on the nitrogen atoms connected to these carbons (Scheme S2 in the ESM) [28–30]. The insertion of carbon nanotubes and protonation do not significantly alter the COF's crystalline ordered structure. Yet, protonation reduces the COF's hydrophobicity, further lowering the water contact angle after forming a hierarchically porous structure mediated by carbon nanotubes (Fig. 2(e)), indicating improved water accessibility. Additionally, protonation reduces the material's surface negative charge. Especially in the presence of carbon nanotubes, possibly due to the exposed larger external surface from the formed hierarchically porous structure, which enlarges the protonation area, leading to even positive surface charges on CNT@COF-H (Fig. S6 in the ESM). All these results demonstrate that the protonated imine-linked triazine-based COF can uniformly cover carbon nanotubes, mediating the formation of a hydrophilic three-dimensional network structure. This architecture facilitates the acquisition of reactants such as O_2 from aqueous environments, thereby enhancing catalytic efficiency.

Subsequently, the optical properties of the composite were investigated. The COF exhibits strong absorption in the ultraviolet region. After protonation, its absorption edge shifts red. By incorporating carbon nanotubes, the CNT@COF-H composite exhibits significant light absorption across the entire ultraviolet-visible-near infrared spectrum (Fig. 3(a)). Correspondingly, Tauc plots derived from the Kubelka–Munk equation indicate that protonation adjusted the COF's bandgap from 2.31 to 1.72 eV, explaining the extended visible absorption of COF-H (Fig. 3(b)). This could be affirmed by density functional theory (DFT) calculations, which also showed the consistent trend of bandgap adjustments with the UV–Vis data (Table S3 in the ESM). According to previous reports, crystalline COFs, especially triazine-based COFs, possess separated charge centers, i.e., electron acceptors from its triazine center and donors from the DMTP monomer, capable of absorbing light energy to produce

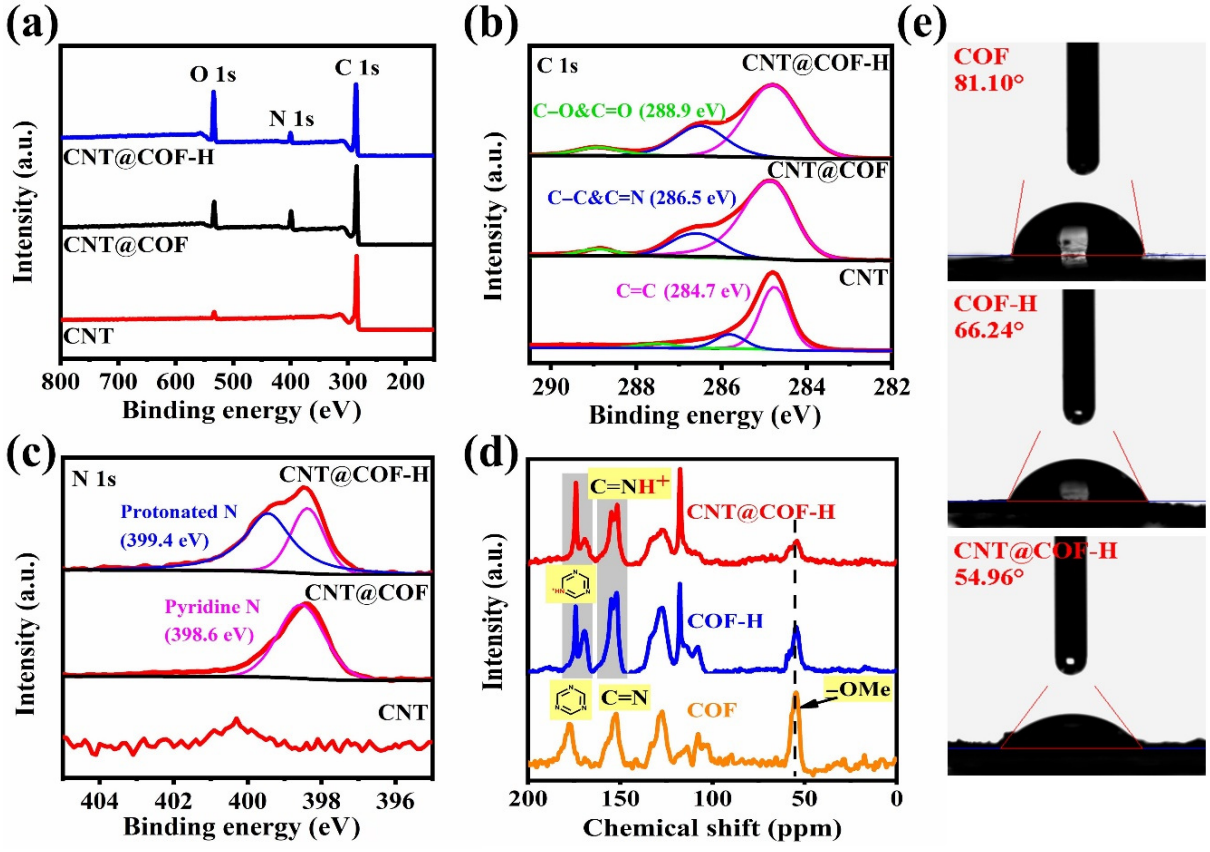

Figure 2 (a) XPS survey spectra and corresponding (b) C 1s and (c) N 1s high-resolution spectra of different materials. (d) Solid-state ^{13}C NMR of different counterparts. (e) Water contact angles of COF, COF-H, and CNT@COF-H, respectively.

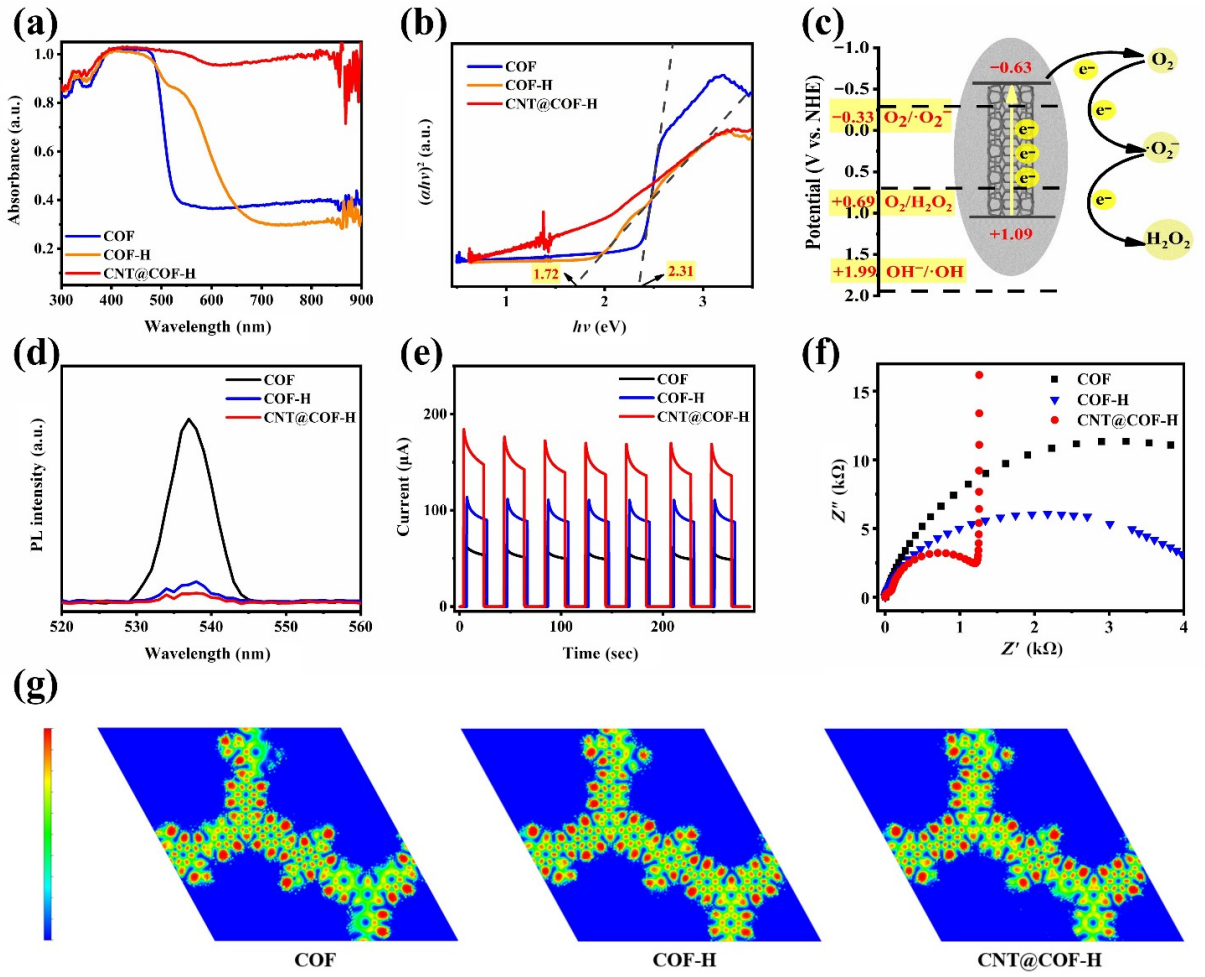

Figure 3 (a) UV–Vis–NIR diffuse reflectance spectrum and (b) corresponding plots of Kubelka–Munk function with calculated band gaps of different materials. (c) Schematic electron transfer from the valence band to conduction band of CNT@COF-H for H_2O_2 generation. (d) PL spectra, (e) photocurrent response maps, (f) EIS maps, and (g) the electron localization function (ELF) of different materials, respectively.

electron–hole pairs for photocatalytic reactions [31]. Consequently, employing the Mott–Schottky analysis, the flat band potential of the COF was calculated to be −0.91eV. Upon protonation, it shifted to −0.83 eV (Fig. S7 in the ESM). Accordingly, the valence band maximum (VBM) and the conduction band minimum (CBM) of COF-H coating on CNT were calculated to be 1.09 and −0.63 eV, respectively (Fig. 3(c)) [32, 33]. This theoretically enables the photocatalytic single-electron two-step reduction of oxygen to generate H_2O_2 ($O_2 + e^- \rightarrow \cdot O_2^-$, $\cdot O_2^- + e^- + 2H^+ \rightarrow H_2O_2$) [34]. Furthermore, the introduction of protonation and carbon nanotubes significantly diminished the photoluminescence intensity of the COF (Fig. 3(d)), particularly the fluorescence intensity of CNT@COF-H at 537 nm, which nearly vanished. Simultaneously, the photocurrent signal of the COF under sunlight excitation incrementally increased with the introduction of protonation and carbon nanotubes (Fig. 3(e)). These outcomes suggest that the protonated COF triazine centers exhibit superior electron-withdrawing ability as advanced electron acceptors, capable of reducing the rate of electron–hole recombination [35]. The incorporation of carbon nanotubes accelerates the transfer of photogenerated electrons, minimizing charge accumulation, further enhancing the separation of electron–hole pairs, and amplifying the photocurrent response [36]. Additionally, electrochemical impedance spectroscopy (EIS) revealed that CNT@COF-H possesses the minimal electron transfer resistance, indicating the highest rate of interfacial charge transfer and an enhanced photocatalytic activity as shown in Fig. 3(f). Moreover, DFT calculations of the local charge density indicated the enhanced electron delocalization in the protonated triazine center of COF-H (Fig. 3(g)), while the extended π–π conjugation via incorporating CNT into COF-H coating allows for further enhancement of the electron delocalization, which facilitated the accelerated migration of free electrons in the active sites [37]. This is conducive to the separation of photogenerated charges, reduction in recombination, and improvement in the photo-electrocatalytic efficiency of the material. These results can be interpreted as the protonated COF triazine centers possessing superior electronegativity, which can lower the rate of electron–hole recombination, while the introduction of carbon nanotubes can expedite the transfer of photogenerated electrons, reduce charge accumulation, further enhance the separation of electron–hole pairs, and strengthen the photocurrent response.

Owing to the CNT@COF-H material's efficient photogenerated charge production efficiency and its theoretical potential for single-electron two-step oxygen reduction to generate H_2O_2, we anticipate it to be an exemplary photocatalyst for the generation of H_2O_2. To corroborate this, its actual photocatalytic H_2O_2 production capability was assessed under simulated sunlight. As anticipated, the

COF was capable of steadily producing H_2O_2 under solar illumination, and its photocatalytic H_2O_2 production capability was significantly enhanced through protonation modification and the introduction of CNT. Under one sun illumination (Fig. 4(a), and Fig. S8 in the ESM), the CNT@COF-H photocatalytically produced H_2O_2 with an efficiency reaching a maximum of 790.528 $\mu M \cdot h^{-1}$, markedly surpassing many previously reported COF-based photocatalysts (Table S4 in the ESM). Moreover, the CNT@COF-H exhibited commendable stability in photocatalytic H_2O_2 production, with no degradation in its capability after five consecutive catalytic cycles (Fig. 4(b)). Furthermore, the bonding structure, crystallinity, and microscopic morphology of CNT@COF-H remained unchanged after the catalytic cycles (Figs. S9–S11 in the ESM), further attesting to its excellent catalytic stability, favorable for practical applications. Concurrently, the apparent quantum yield (AQY) of the CNT@COF-H composite under different wavelength excitations was examined (Fig. 4(c)), revealing that at 500 nm, CNT@COF-H achieved a maximum AQY of 34%, demonstrating optimal photocatalytic performance at this wavelength. However, due to the introduction of carbon nanotubes, the CNT@COF-H composite maintained a quantum efficiency of over 2% at wavelengths greater than 500 nm, even up to 800 nm, indicating its effective utilization of sunlight for photocatalytic reactions. Specifically, under one sun irradiation of 5 mg CNT@COF-H composite for 60 min, and the reaction solution was collected. H_2O_2 in the reaction solution was able to degrade the colored environmental organic dye pollutant of rhodamine B (10 $mg \cdot L^{-1}$) into a colorless solution within 200 s in the presence of Fe^{2+} (Fig. 4(h), and Figs. S16 and S17 in the ESM) [38]. Furthermore, a solution of H_2O_2 produced by 60 min of sunlight excitation of the CNT@COF-H composite significantly inhibited the growth of *Escherichia coli* (*E. coli*) and *Staphylococcus aureus* (*S. aureus*). The antibacterial capability was further enhanced upon the addition of a solution containing Fe^{2+}, due to the generation of hydroxyl radicals through the Fenton reaction. Co-incubation demonstrated that the antibacterial efficiency against *E. coli* and *S. aureus* could respectively reach 75% and 92% (Fig. 4(i), and Fig. S18 in the ESM). These findings also attest to the potential applications of photocatalytically generated H_2O_2 based on CNT@COF-H in pollutant treatment and antibacterial efforts, representing an

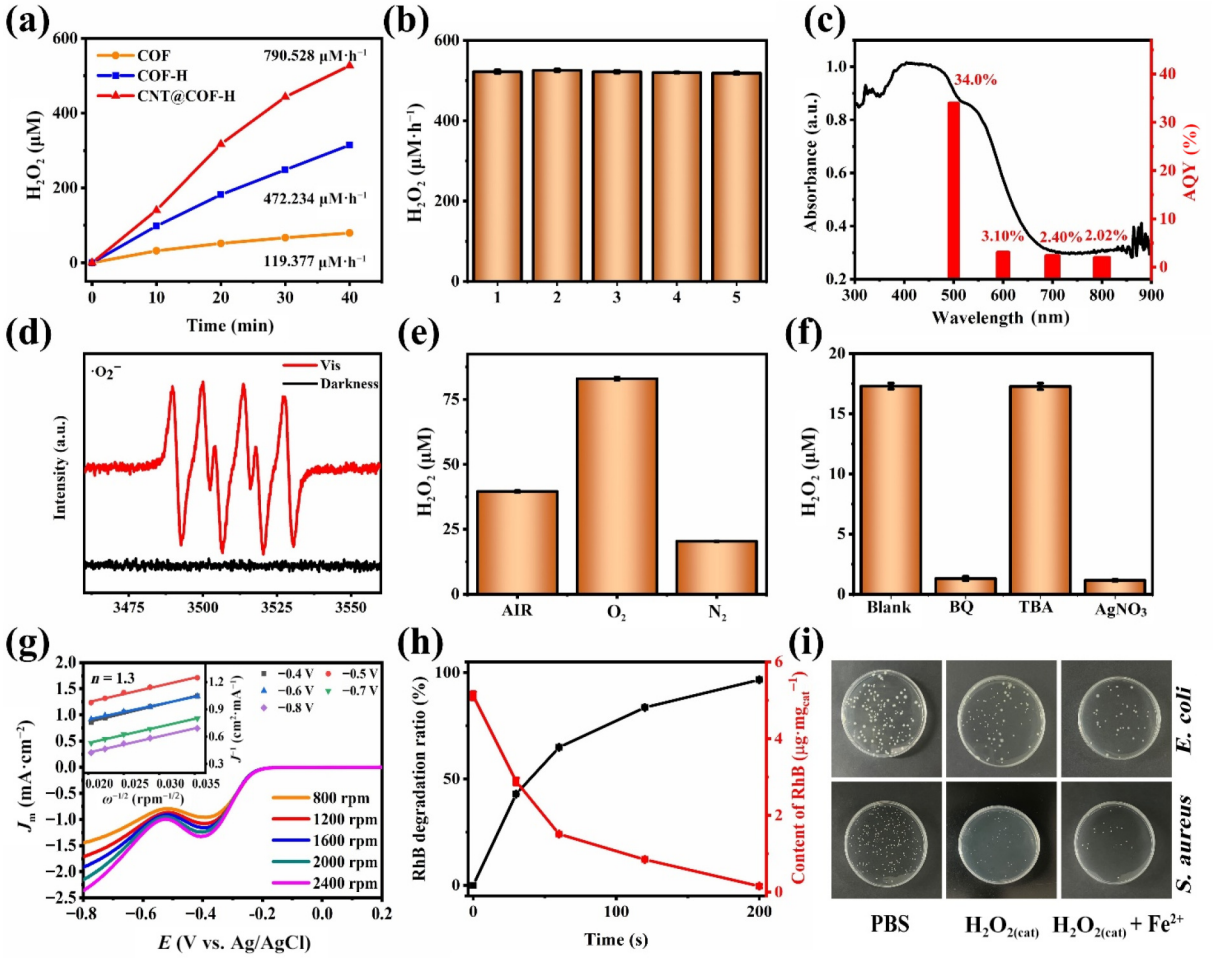

Figure 4 (a) H_2O_2 production curves of different materials upon a stimulated sunlight irradiation (0.1 $W \cdot cm^{-2}$) for different time periods. (b) Comparisons of H_2O_2 yields over five cycles for 5 mg CNT@COF-H dispersed in 10 mL aqueous solution under a stimulated sunlight irradiation (0.1 $W \cdot cm^{-2}$) for 40 min. (c) Apparent quantum yields of CNT@COF-H for H_2O_2 generation at different wavelengths. (d) EPR plots for CNT@COF-H under different conditions. (e) Comparisons of photocatalytic H_2O_2 generating capacity of CNT@COF-H in aqueous solutions with different atmospheres. (f) Comparisons of photocatalytic H_2O_2 generation capacity of CNT@COF-H after addition of different radical trapping agents. (g) LSV scanning curves of CNT@COF-H for ORR experiments. (h) Degradation of rhodamine B via the produced H_2O_2 by CNT@COF-H under the Fe^{2+} assisted Fenton reaction. (i) Photographs of agar plates of *E. coli* and *S. aureus* bacteria incubated with the different solutions for 12 h at 37 °C. The solutions were phosphate buffer saline, the produced H_2O_2 solution by CNT@COF-H, and the mixed solution of Fe^{2+} with the produced H_2O_2, respectively. All data are presented as means ±SD (n = 3).

excellent, sustainable catalyst for environmental remediation.

To investigate the mechanism behind the photocatalytic generation of H_2O_2 by CNT@COF-H, intermediates of the photocatalytic reaction were examined using electron paramagnetic resonance (EPR). As depicted in Fig. 4(d), the presence of $\cdot O_2^-$ intermediates during the CNT@COF-H photocatalytic reaction indicates the involvement of O_2, likely through the acquisition of an electron to form the superoxide anion. Further, the capability of photocatalytically producing H_2O_2 under different atmospheric conditions was assessed (Fig. 4(e), and Fig. S12 in the ESM), revealing that in an oxygen-containing atmosphere, particularly in a solution saturated with pure oxygen, CNT@COF-H demonstrated the strongest ability to catalyze the production of H_2O_2. This further elucidates that the photocatalytic reduction reaction involving oxygen primarily generates H_2O_2, proceeding via a single-electron two-step reduction process with the superoxide anion as the intermediate. Since this process necessitates an adequate supply of H^+ to combine with the superoxide anion to form H_2O_2, CNT@COF-H exhibits a heightened capability to photocatalytically produce H_2O_2 at lower pH levels (Fig. S13 in the ESM). Moreover, the impacts of using scavengers such as p-benzoquinone, tert-butanol, and $AgNO_3$ to trap $\cdot O_2^-$, $\cdot OH$, and e^-, respectively, on the H_2O_2 production by CNT@COF-H were investigated (Fig. 4(f), and Fig. S14 in the ESM). It was discovered that the addition of $\cdot OH$ scavengers did not significantly alter the amount of H_2O_2 generated, whereas the inclusion of $\cdot O_2^-$ and e^- scavengers markedly decreased H_2O_2 production, reaffirming that the single-electron two-step reduction process with the superoxide anion as the intermediate is the predominant pathway for CNT@COF-H photocatalytic H_2O_2 generation (Fig. 3(c)). This process, utilizing oxygen as the reactant substrate, was found through rotating disk electrode (RDE) testing to be influenced by oxygen diffusion, with catalytic activity significantly enhanced under higher rotation speeds (faster oxygen diffusion). Accordingly, the average number of electron transfers (n) calculated for the catalyst was 1.3, indicating that the photocatalytic generation of H_2O_2 primarily follows a single-electron process. Notably, the electron transfer number being slightly above 1, in conjunction with the results shown in Fig. 3(c), suggests that besides the primary single-electron two-step reduction to generate H_2O_2, CNT@COF-H may also facilitate a minor pathway through a direct two-electron reduction of oxygen to produce H_2O_2. This process efficiently utilizes the electrons generated by the photoelectric effect of CNT@COF-H, and with the addition of isopropanol (IPA) as a hole scavenger, the efficiency of electron utilization and consequently, the yield of H_2O_2, can be further increased (Fig. S15 in the ESM).

Finally, the spatial distribution of photoexcited electrons and holes for functionalized COF materials was investigated by DFT computational analysis (Fig. 5(a)). Compared to the pristine COF, the charge distribution of the conduction band and valence band in the protonated COF-H is more separated, with the conduction band charge (predominantly electrons) primarily concentrated at the protonated triazine centers, and the valence band charge (predominantly holes) mainly distributed across the imine bonds and the phenyl rings of the COF framework. Within the CNT@COF-H composite material, the conduction band electrons are further transferred onto the carbon nanotubes, demonstrating that CNTs, as electron transporters, can accept photogenerated electrons, thus accelerating electron transfer and reducing carrier recombination. On this basis, the energy diagram for the reduction reaction was calculated. As depicted in Fig. 5(b) and Fig. S20 in the ESM, protonated versions of COF-H and CNT@COF-H facilitate the catalysis of O_2 to form the superoxide anion transition state more readily, which further combines with protons to form $*H_2O_2$. $*H_2O_2$ is then converted to H_2O_2, a transformation that represents the rate-determining step of the entire reaction, with the reaction barriers for COF, COF-H, and CNT@COF-H being 0.4, 0.4, and 0.19 eV, respectively. This indicates that the introduction of protonation and carbon nanotubes renders CNT@COF-H most favorable for promoting the generation of H_2O_2. All these findings suggest that CNT@COF-H, by photocatalytically reducing O_2 to $\cdot O_2^-$ and further combining it with H^+ to reduce it to H_2O_2, serves as an excellent single-electron two-step oxygen reduction photocatalyst, conducive to low-cost and sustainable H_2O_2 production.

4 Conclusions

In conclusion, CNT@COF-H nanocomposite was prepared by *in-*

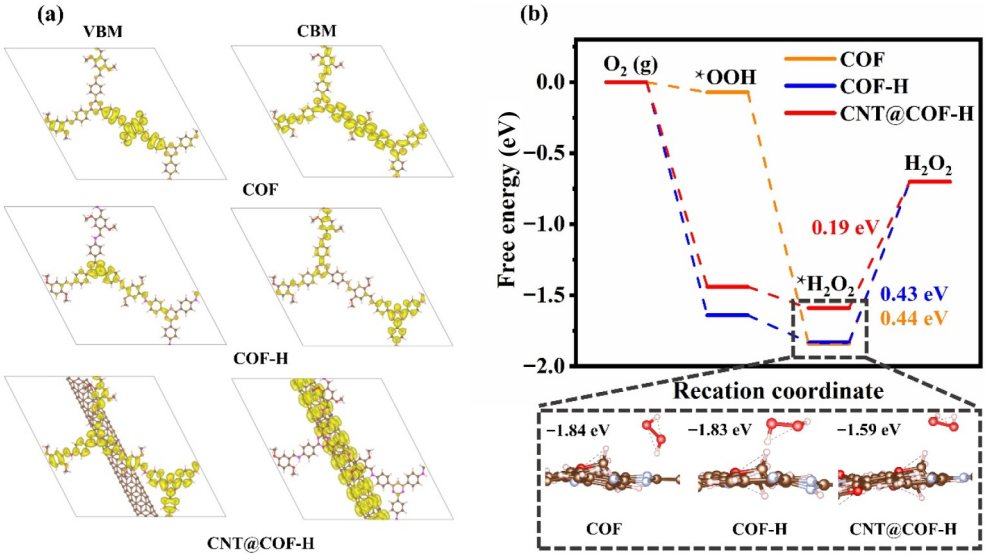

Figure 5 (a) Distributions of theVBM and CBM for the model system of COF, COF-H, and CNT@COF-H, respectively. (b) Free energy profiles for photocatalytic H_2O_2 evolution reactions over COF, COF-H, and CNT@COF-H, respectively.

situ growth of imine-linked triazine-based COF on CNT and then protonation in the acidic solution. This nanocomposite ensures a strong interface between the COF and CNT, and combines the desirable properties of both components. The incorporated CNT could serve as an electron transporter to broaden the light adsorption and decrease the electron–hole pair recombination of COF via increasing the electronic delocalization. Meanwhile, the protonation of imine further regulated the energy bands of COF and simultaneously ensured its substrate accessibility via an increase the hydrophilicity. Thus, the synergistic integration of protonated COF and CNT creates an efficient and durable material for photocatalytic H_2O_2 generation. Herein, its performance surpasses those of pristine COFs and many other reported COF-based systems, exhibiting important applications in obvious sterilization and apparent dye degradation. This CNT@COF-H nanocomposite promises a sustainable and cost-effective approach to harnessing solar energy for the chemical synthesis of H_2O_2, paving the way for greener and more efficient industrial processes.

Electronic Supplementary Material: Supplementary material (material characterization, testing methods, calculation methods, photographs of experimental, scanning electron microscopy images, transmission electron microscopy images, nitrogen adsorption–desorption curves, Fourier transform infrared spectra, XRD pattern, UV–Vis spectra, zeta potential, H_2O_2 detection, rhodamine B degradation, survival ratios of *E. coli* and *S. aureus*, and DFT calculation) is available in the online version of this article at https://doi.org/10.26599/NR.2025.94907024.

Data availability

All data needed to support the conclusions in the paper are presented in the manuscript and the Electronic Supplementary Material. Additional data related to this paper may be requested from the corresponding author upon request.

Acknowledgements

This work was supported by the Natural Science Foundation of Shanghai (No. 20ZR1401800).

Declaration of competing interest

All the contributing authors report no conflict of interests in this work.

Author contribution statement

L. Y. Y.: Data curation, writing manuscript, experimental design. W. X. L.: Data curation, experimental design. Y. Y. W.: Data curation, experimental design. Y. W.: Project administration, funding acquisition, experimental design, writing manuscript. All the authors have approved the final manuscript.

Use of AI statement

None.

References

[1] Lu, Z. Y.; Chen, G. X.; Siahrostami, S.; Chen, Z. H.; Liu, K.; Xie, J.; Liao, L.; Wu, T.; Lin, D. C.; Liu, Y. Y. et al. High-efficiency oxygen reduction to hydrogen peroxide catalysed by oxidized carbon materials. *Nat. Catal.* **2018**, *1*, 156–162.

[2] Perry, S. C.; Pangotra, D.; Vieira, L.; Csepei, L. I.; Sieber, V.; Wang, L.; de León, C. P.; Walsh, F. C. Electrochemical synthesis of hydrogen peroxide from water and oxygen. *Nat. Rev. Chem.* **2019**, *3*, 442–458.

[3] Li, X. G.; Tang, S. S.; Dou, S.; Fan, H. J.; Choksi, T. S.; Wang, X. Molecule confined isolated metal sites enable the electrocatalytic synthesis of hydrogen peroxide. *Adv. Mater.* **2022**, *34*, 2104891.

[4] Bu, Y. F.; Wang, Y. B.; Han, G. F.; Zhao, Y. X.; Ge, X. L.; Li, F.; Zhang, Z. H.; Zhong, Q.; Baek, J. B. Carbon-based electrocatalysts for efficient hydrogen peroxide production. *Adv. Mater.* **2021**, *33*, 2103266.

[5] Kim, H. W.; Ross, M. B.; Kornienko, N.; Zhang, L.; Guo, J. H.; Yang, P. D.; McCloskey, B. D. Efficient hydrogen peroxide generation using reduced graphene oxide-based oxygen reduction electrocatalysts. *Nat. Catal.* **2018**, *1*, 282–290.

[6] Sun, Y. Y.; Han, L.; Strasser, P. A comparative perspective of electrochemical and photochemical approaches for catalytic H_2O_2 production. *Chem. Soc. Rev.* **2020**, *49*, 6605–6631.

[7] Xue, Y. D.; Wang, Y. T.; Pan, Z. H.; Sayama, K. Electrochemical and photoelectrochemical water oxidation for hydrogen peroxide production. *Angew. Chem., Int. Ed.* **2021**, *60*, 10469–10480.

[8] Freese, T.; Meijer, J. T.; Feringa, B. L.; Beil, S. B. An organic perspective on photocatalytic production of hydrogen peroxide. *Nat. Catal.* **2023**, *6*, 553–558.

[9] Li, M.; Zhang, S. B. Coupling waste plastic upgrading and CO_2 photoreduction to high-value chemicals by a binuclear Re–Ru heterogeneous catalyst. *ACS Catal.* **2024**, *14*, 6717–6727.

[10] Li, M.; Zhang, S. B. Tandem chemical depolymerization and photoreforming of waste PET plastic to high-value-added chemicals. *ACS Catal.* **2024**, *14*, 2949–2958.

[11] Huang, N. Y.; Zheng, Y. T.; Chen, D.; Chen, Z. Y.; Huang, C. Z.; Xu, Q. Reticular framework materials for photocatalytic organic reactions. *Chem. Soc. Rev.* **2023**, *52*, 7949–8004.

[12] Guo, Y.; Tong, X. L.; Yang, N. J. Photocatalytic and electrocatalytic generation of hydrogen peroxide: Principles, catalyst design and performance. *Nano-Micro Lett.* **2023**, *15*, 77.

[13] Li, H. X.; Li, R. J.; Liu, G.; Zhai, M. L.; Yu, J. G. Noble-metal-free single- and dual-atom catalysts for artificial photosynthesis. *Adv. Mater.* **2024**, *36*, 2301307.

[14] Kondo, Y.; Kuwahara, Y.; Mori, K.; Yamashita, H. Design of metal-organic framework catalysts for photocatalytic hydrogen peroxide production. *Chem* **2022**, *8*, 2924–2938.

[15] Yu, X. H.; Hu, Y. P.; Shao, C. C.; Huang, W.; Li, Y. G. Polymer semiconductors: A unique platform for photocatalytic hydrogen peroxide production. *Mater. Today* **2023**, *71*, 152–173.

[16] Wang, H.; Wang, H.; Wang, Z. W.; Tang, L.; Zeng, G. M.; Xu, P.; Chen, M.; Xiong, T.; Zhou, C. Y.; Li, X. Y. et al. Covalent organic framework photocatalysts: Structures and applications. *Chem. Soc. Rev.* **2020**, *49*, 4135–4165.

[17] Liu, R. Y.; Chen, Y. Z.; Yu, H. D.; Položij, M.; Guo, Y. Y.; Sum, T. C.; Heine, T.; Jiang, D. L. Linkage-engineered donor-acceptor covalent organic frameworks for optimal photosynthesis of hydrogen peroxide from water and air. *Nat. Catal.* **2024**, *7*, 195–206.

[18] Yong, Z. J.; Ma, T. Y. Solar-to-H_2O_2 catalyzed by covalent organic frameworks. *Angew. Chem., Int. Ed.* **2023**, *62*, e202308980.

[19] Liang, A. J.; Li, W. B.; Li, A. B.; Peng, H.; Ma, G. F.; Zhu, L.; Lei, Z. Q.; Xu, Y. X. Covalent triazine frameworks materials for photo- and electro-catalysis. *Nano Res.* **2024**, *17*, 7830–7839.

[20] Liu, R. Y.; Tan, K. T.; Gong, Y. F.; Chen, Y. Z.; Li, Z. E.; Xie, S. L.; He, T.; Lu, Z.; Yang, H.; Jiang, D. L. Covalent organic frameworks: An ideal platform for designing ordered materials and advanced applications. *Chem. Soc. Rev.* **2021**, *50*, 120–242.

[21] Ren, X. T.; Sun, J. J.; Li, Y. S.; Bai, F. Primitive functional groups directed distinct photocatalytic performance of imine-linked donor-

acceptor covalent organic frameworks. *Nano Res.* **2024**, *17*, 4994–5001.

[22] Liu, Y.; Shi, Y. W.; Wang, H.; Zhang, S. B. Donor-acceptor covalent organic frameworks-confined ultrafine bimetallic Pt-based nanoclusters for enhanced photocatalytic H_2 generation. *Nano Res.* **2024**, *17*, 5835–5844.

[23] Liu, Y. K.; Liu, X. A.; Su, A.; Gong, C. T.; Chen, S. W.; Xia, L. W.; Zhang, C. W.; Tao, X. H.; Li, Y.; Li, Y. H. et al. Revolutionizing the structural design and determination of covalent-organic frameworks: Principles, methods, and techniques. *Chem. Soc. Rev.* **2024**, *53*, 502–544.

[24] Liao, Y. X.; Guo, L. C.; Gong, L. L.; Zhang, Q. Y.; Zhao, D.; Jia, Y. Z.; Hua, R.; Luo, F. Regulating benzene ring number as connector in covalent organic framework for boosting photosynthesis of H_2O_2 from seawater. *Nano Lett.* **2024**, *24*, 3819–3825.

[25] Feng, C. Y.; Wu, Z. P.; Huang, K. W.; Ye, J. H.; Zhang, H. B. Surface modification of 2D photocatalysts for solar energy conversion. *Adv. Mater.* **2022**, *34*, 2200180.

[26] Yang, L. J.; Chen, Z. X.; Cao, Q.; Liao, H. R.; Gao, J.; Zhang, L.; Wei, W. Y.; Li, H.; Lu, J. M. Structural regulation of photocatalyst to optimize hydroxyl radical production pathways for highly efficient photocatalytic oxidation. *Adv. Mater.* **2024**, *36*, 2306758.

[27] Qian, Y. Y.; Han, Y. L.; Zhang, X. Y.; Yang, G.; Zhang, G. Z.; Jiang, H. L. Computation-based regulation of excitonic effects in donor-acceptor covalent organic frameworks for enhanced photocatalysis. *Nat. Commun.* **2023**, *14*, 3083.

[28] Shi, T.; Wang, H.; Li, L.; Zhao, Z.; Wang, C. M.; Zhang, X. D.; Xie, Y. Enhanced photostability in protonated covalent organic frameworks for singlet oxygen generation. *Matter* **2022**, *5*, 1004–1015.

[29] Zhu, Q.; Shi, L.; Li, Z.; Li, G. S.; Xu, X. X. Protonation of an imine-linked covalent organic framework for efficient H_2O_2 photosynthesis under visible light up to 700 nm. *Angew. Chem., Int. Ed.* **2024**, *63*, e202408041.

[30] Guerrini, M.; Delgado Aznar, E.; Cocchi, C. Electronic and optical properties of protonated triazine derivatives. *J. Phys. Chem. C* **2020**, *124*, 27801–27810.

[31] Yang, J.; Acharjya, A.; Ye, M. Y.; Rabeah, J.; Li, S.; Kochovski, Z.; Youk, S.; Roeser, J.; Grüneberg, J.; Penschke, C. et al. Protonated imine-linked covalent organic frameworks for photocatalytic hydrogen evolution. *Angew. Chem., Int. Ed.* **2021**, *60*, 19797–19803.

[32] Yang, H.; He, D. Y.; Zhang, T. T.; Liu, C. H.; Cheng, F. Y.; Zhou, Y. J.; Zhang, Y. N.; Qu, J. Magnetic carbon nanotubes/red phosphorus/graphitic carbon nitride heterojunction for highly efficient visible-light photocatalytic water disinfection. *Chem. Eng. J.* **2023**, *466*, 143309.

[33] Lin, L. H.; Ma, Y. W.; Zettsu, N.; Vequizo, J. J. M.; Gu, C.; Yamakata, A.; Hisatomi, T.; Takata, T.; Domen, K. Carbon nanotubes as a solid-state electron mediator for visible-light-driven Z-scheme overall water splitting. *J. Am. Chem. Soc.* **2024**, *146*, 14829–14834.

[34] He, F. T.; Lu, Y. M.; Wu, Y. Z.; Wang, S. L.; Zhang, Y.; Dong, P.; Wang, Y. Q.; Zhao, C. C.; Wang, S. J.; Zhang, J. Q. et al. Rejoint of carbon nitride fragments into multi-interfacial order-disorder homojunction for robust photo-driven generation of H_2O_2. *Adv. Mater.* **2024**, *36*, 2307490.

[35] Kulkarni, R.; Noda, Y.; Kumar Barange, D.; Kochergin, Y. S.; Lyu, P.; Balcarova, B.; Nachtigall, P.; Bojdys, M. J. Real-time optical and electronic sensing with a β-amino enone linked, triazine-containing 2D covalent organic framework. *Nat. Commun.* **2019**, *10*, 3228.

[36] Ning, R.; Kim, S.; Sun, E.; Jiang, Y.; Baek, J.; Li, Y. Z.; Robinson, A.; Vallez, L.; Zheng, X. L. Enhanced H_2O_2 upcycling into hydroxyl radicals with GO/Ni: FeOOH-coated silicon nanowire photocatalysts for wastewater treatment. *Nano Lett.* **2023**, *23*, 6323–6329.

[37] Zhao, Y. L.; Xu, X. H.; Zhang, K. N.; Li, Z. Y.; Wang, H. Y.; Zhao, Y.; Qiu, J. K.; Wang, J. J. Designing local electron delocalization in 2D covalent organic frameworks for enhanced sunlight-driven photocatalytic activity. *ACS Catal.* **2024**, *14*, 3556–3564.

[38] Ren, X. T.; Wen, M. Y.; Hou, X. B.; Sun, J. J.; Bai, F.; Li, Y. S. Covalent organic framework isomers with divergent photocatalytic properties. *Chem. Commun.* **2024**, *60*, 4423–4426.